PHYSICAL REVIEW D VOLUME 45, NUMBER 7 1 APRIL 1992

Properties of events with large total transverse energy produced in proton-antiproton collisions at $\sqrt{s} = 1.8$ TeV

F. Abe,[i] D. Amidei,[d] G. Apollinari,[p] M. Atac,[d] P. Auchincloss,[o] A. R. Baden,[f]
N. Bacchetta,[k] M. W. Bailey,[n] A. Bamberger,[d,*] P. de Barbaro,[o] B. A. Barnett,[h] A. Barbaro-Galtieri,[j] V. E. Barnes,[n]
T. Baumann,[f] F. Bedeschi,[m] S. Behrends,[b] S. Belforte,[m] G. Bellettini,[m] J. Bellinger,[u] D. Benjamin,[t]
J. Bensinger,[b] A. Beretvas,[d] J. P. Berge,[d] S. Bertolucci,[e] S. Bhadra,[g] M. Binkley,[d] R. Blair,[a]
C. Blocker,[b] V. Bolognesi,[m] A. W. Booth,[d] C. Boswell,[h] G. Brandenburg,[f] D. Brown,[f] E. Buckley-Geer,[q]
H. S. Budd,[o] G. Busetto,[k] A. Byon-Wagner,[d] K. L. Byrum,[u] C. Campagnari,[c] M. Campbell,[c] A. Caner,[d]
R. Carey,[f] W. Carithers,[j] D. Carlsmith,[u] J. T. Carroll,[d] R. Cashmore,[d,*] A. Castro,[k] F. Cervelli,[m]
K. Chadwick,[d] G. Chiarelli,[e] W. Chinowsky,[j] S. Cihangir,[d] A. G. Clark,[d] D. Connor,[l] M. Contreras,[b]
J. Cooper,[d] M. Cordelli,[e] D. Crane,[d] M. Curatolo,[e] C. Day,[d] F. DeJongh,[d] S. Dell'Agnello,[m]
M. Dell'Orso,[m] L. Demortier,[b] B. Denby,[d] P. F. Derwent,[c] T. Devlin,[q] D. DiBitonto,[r] M. Dickson,[o]
R. B. Drucker,[j] K. Einsweiler,[j] J. E. Elias,[d] R. Ely,[j] S. Eno,[c] S. Errede,[g] B. Esposito,[e]
B. Flaugher,[d] G. W. Foster,[d] M. Franklin,[f] J. Freeman,[d] H. Frisch,[c] T. Fuess,[d] Y. Fukui,[i]
Y. Funayama,[s] A. F. Garfinkel,[n] A. Gauthier,[g] S. Geer,[d] D. W. Gerdes,[c] P. Giannetti,[m] N. Giokaris,[p]
P. Giromini,[e] L. Gladney,[l] M. Gold,[j] K. Goulianos,[p] H. Grassmann,[k] C. Grosso-Pilcher,[c] C. Haber,[j]
S. R. Hahn,[d] R. Handler,[u] K. Hara,[s] R. M. Harris,[d] J. Hauser,[d] C. Hawk,[q] T. Hessing,[r]
R. Hollebeek,[l] L. Holloway,[g] P. Hu,[q] B. Hubbard,[j] B. T. Huffman,[n] R. Hughes,[l] P. Hurst,[e]
J. Huth,[d] J. Hylen,[d] M. Incagli,[m] T. Ino,[s] H. Iso,[s] H. Jensen,[d] C. P. Jessop,[f]
R. P. Johnson,[d] U. Joshi,[d] R. W. Kadel,[j] T. Kamon,[r] S. Kanda,[s] D. A. Kardelis,[g] I. Karliner,[g]
E. Kearns,[f] L. Keeble,[r] R. Kephart,[d] P. Kesten,[b] R. M. Keup,[g] H. Keutelian,[d] D. Kim,[d]
S. Kim,[s] L. Kirsch,[b] K. Kondo,[s] J. Konigsberg,[f] E. Kovacs,[d] S. E. Kuhlmann,[a] E. Kuns,[q]
A. T. Laasanen,[n] J. I. Lamoureux,[u] S. Leone,[m] W. Li,[a] P. Limon,[d] T. M. Liss,[g] N. Lockyer,[l]
C. B. Luchini,[g] P. Lukens,[d] P. Maas,[u] K. Maeshima,[d] M. Mangano,[m] J. P. Marriner,[d] M. Mariotti,[m]
R. Markeloff,[u] L. A. Markosky,[u] R. Mattingly,[b] P. McIntyre,[r] A. Menzione,[m] T. Meyer,[r] S. Mikamo,[i]
M. Miller,[c] T. Mimashi,[s] S. Miscetti,[e] M. Mishina,[i] S. Miyashita,[s] Y. Morita,[s] S. Moulding,[b]
J. Mueller,[q] A. Mukherjee,[d] L. F. Nakae,[b] I. Nakano,[s] C. Nelson,[d] C. Newman-Holmes,[d] J. S. T. Ng,[f]
M. Ninomiya,[s] L. Nodulman,[a] S. Ogawa,[s] R Paoletti,[m] A. Para,[d] E. Pare,[f] S. Park,[d]
J. Patrick,[d] T. J. Phillips,[f] F. Ptohos,[f] R. Plunkett,[d] L. Pondrom,[u] J. Proudfoot,[a] G. Punzi,[m]
D. Quarrie,[d] K. Ragan,[l] G. Redlinger,[c] J. Rhoades,[u] M. Roach,[t] F. Rimondi,[d,*] L. Ristori,[m]
T. Rohaly,[l] A. Roodman,[c] W. K. Sakumoto,[o] A. Sansoni,[e] R. D. Sard,[g] A. Savoy-Navarro,[d] V. Scarpine,[g]
P. Schlabach,[f] E. E. Schmidt,[d] O. Schneider,[j] M. H. Schub,[n] R. Schwitters,[f] A. Scribano,[m] S. Segler,[d]
Y. Seiya,[s] M. Sekiguchi,[s] M. Shapiro,[j] N. M. Shaw,[n] M. Sheaff,[u] M. Shochet,[c] J. Siegrist,[j]
P. Sinervo,[n] J. Skarha,[h] K. Sliwa,[t] D. A. Smith,[m] F. D. Snider,[h] L. Song,[l] M. Spahn,[j]
R. St. Denis,[f] A. Stefanini,[m] G. Sullivan,[c] R. L. Swartz, Jr.,[g] M. Takano,[s] F. Tartarelli,[m] K. Takikawa,[s]
S. Tarem,[b] D. Theriot,[d] M. Timko,[r] P. Tipton,[d] S. Tkaczyk,[d] A. Tollestrup,[d] J. Tonnison,[n]
W. Trischuk,[f] N. Turini,[m] Y. Tsay,[c] F. Ukegawa,[s] D. Underwood,[a] S. Vejcik III,[h] R. Vidal,[d]
R. G. Wagner,[a] R. L. Wagner,[d] N. Wainer,[d] J. Walsh,[l] T. Watts,[q] R. Webb,[r] C. Wendt,[u]
H. Wenzel,[m] W. C. Wester III,[j] T. Westhusing,[m] S. N. White,[p] A. B. Wicklund,[a] H. H. Williams,[l] B. L. Winer,[o]
J. Wyss,[k] A. Yagil,[d] A. Yamashita,[s] K. Yasuoka,[s] G. P. Yeh,[d] J. Yoh,[d] M. Yokoyama,[s]
J. C. Yun,[d] A. Zanetti,[m] F. Zetti,[m] and S. Zucchelli[d,*]
(CDF Collaboration)

[a]*Argonne National Laboratory, Argonne, Illinois 60439*
[b]*Brandeis University, Waltham, Massachusetts 02254*
[c]*University of Chicago, Chicago, Illinois 60637*
[d]*Fermi National Accelerator Laboratory, Batavia, Illinois 60510*
[e]*Laboratori Nazionali di Frascati, Istituto Nazionale di Fisica Nucleare, Frascati, Italy*
[f]*Harvard University, Cambridge, Massachusetts 02138*
[g]*University of Illinois, Urbana, Illinois 61801*
[h]*The Johns Hopkins University, Baltimore, Maryland 21218*
[i]*National Laboratory for High Energy Physics (KEK), Japan*
[j]*Lawrence Berkeley Laboratory, Berkeley, California 94720*
[k]*Universita di Padova, Instituto Nazionale di Fisica Nucleare, Sezione di Padova, I-35131 Padova, Italy*
[l]*University of Pennsylvania, Philadelphia, Pennsylvania 19104*
[m]*Istituto Nazionale di Fisica Nucleare, University and Scuola Normale Superiore of Pisa, I-56100 Pisa, Italy*
[n]*Purdue University, West Lafayette, Indiana 47907*
[o]*University of Rochester, Rochester, New York 14627*
[p]*Rockefeller University, New York, New York 10021*

---

[*] Visitor

[q]*Rutgers University, Piscataway, New Jersey 08854*
[r]*Texas A&M University, College Station, Texas 77843*
[s]*University of Tsukuba, Tsukuba, Ibaraki 305, Japan*
[t]*Tufts University, Medford, Massachusetts 02155*
[u]*University of Wisconsin, Madison, Wisconsin 53706*
(Received 22 October 1991)

The properties of proton-antiproton interactions in which the total transverse energy exceeds 400 GeV are described. These events have been recorded at the Fermilab Tevatron collider operating at a center-of-mass energy of 1.8 TeV. The differential cross section, jet rates, jet transverse-momentum and pseudorapidity distributions, single-jet shapes, and the multijet rates and kinematics are compared with QCD predictions. There is no evidence for a significant deviation from standard-model expectations that would be signaled by the presence of an excess of isolated high-transverse-momentum leptons or photons, or an excess of events with unusual jet rates or characteristics.

PACS number(s): 13.87.Ce, 12.38.Qk, 13.85.Rm

I. INTRODUCTION

The Collider Detector at Fermilab [1] (CDF) has taken data at the Fermilab Tevatron proton-antiproton collider operating at a center-of-mass energy of 1.8 TeV. This is the highest $p\bar{p}$ collision energy currently available in the laboratory. In this paper we describe the properties of the events recorded by CDF which have the highest observed total transverse energies:

$$\sum E_T \equiv \sum_i E_i \sin\theta_i > 400 \text{ GeV} ,$$

where the sum is over all calorimeter cells in the detector, E_i is the energy deposition recorded by the ith cell, and the angle θ_i is the angle between the $p\bar{p}$ collision axis and a vector pointing from the interaction vertex to the energy deposition in the ith cell. The data sample corresponds to an integrated luminosity of 4.0 ± 0.3 pb^{-1}. The rates and properties of these events are compared with the predictions of quantum chromodynamics (QCD).

Within the framework of QCD, events with large $\sum E_T$ arise from hard scattering of the constituent partons in the proton and antiproton. The outgoing scattered partons manifest themselves as hadronic jets. The resulting events are therefore expected to contain two jets with large components of momentum transverse to the beam axis (p_T). Higher-order QCD corrections to the basic parton-parton scattering process can give rise to further high-p_T jets in the final state, resulting in more complicated even topologies. The observed $\sum E_T$ spectrum, together with the number and characteristics of the jets observed in the high-$\sum E_T$ event sample, can be compared with expectations to see if the "hottest events" produced in the highest-energy $p\bar{p}$ collisions are described by QCD.

II. THE CDF DETECTOR

The CDF detector, described in detail in Ref. [1], is a general purpose magnetic detector designed to measure high-energy $p\bar{p}$ collisions. In the following a brief description is given of the main detector components relevant to the present analysis. Figure 1 shows a schematic of the detector which provides charged-particle tracking, fine-grained electromagnetic and hadronic calorimetry, and muon detection.

A. Tracking

Immediately outside of the beam pipe a system of eight vertex time projection chambers (VTPC) tracks charged particles at angles greater than 3.5° from the beam axis. The VTPC chambers contain 3072 sense wires and 3072 pads for measurement of track coordinates projected onto the R-Z and R-ϕ planes, respectively, where R is the radial distance from the beam line, Z is the distance along the beam line from the detector center, and ϕ is the azimuthal angle. The VTPC is 2.8 m long giving good coverage of the interaction region ($\sigma_Z = 30$ cm). The active region of the chambers extends from $R = 6.8$ cm to $R = 21$ cm, and provides a single-hit precision of 200–500 μm, and a two-track resolution of 6 mm in the R-Z plane. This enables the interaction vertex to be accurately located, and events with two primary vertices to be recognized with good efficiency.

At larger radii the central tracking chamber (CTC) provides a precision momentum determination of charged particles. Track curvature is measured in a uniform 1.41-T solenoidal magnetic field coaxial with the beam axis. The CTC is a 3.2-m-long cylindrical drift chamber with a radius of 1.3 m, and covers the angular interval $40° < \theta < 140°$, where θ is the polar angle. This corresponds to the pseudorapidity interval $|\eta| < 1$, where $\eta \equiv -\ln(\tan\theta/2)$. The CTC contains 84 layers of sense wires grouped into nine superlayers. Five of the superlayers consist of 12 axial sense wire layers, the other four superlayers consist of six layers of sense wires tilted by ±3° relative to the beam direction. The chamber provides a momentum resolution of $\delta p_T/p_T^2 \leq 0.002$ (GeV/c)$^{-1}$ for isolated charged tracks.

B. Calorimetry

The CDF calorimeters are constructed in a tower geometry and cover the region $|\eta| < 4.2$. The coverage of

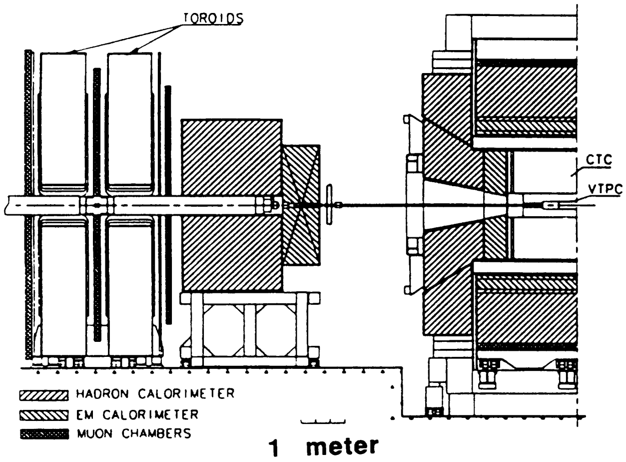

FIG. 1. A cut-away view through the forward half of CDF. The detector is forward-backward symmetric about the interaction point.

the calorimeter towers in η-ϕ space is shown in Fig. 2. Each tower has an electromagnetic (EM) calorimeter cell at the front and a hadronic calorimeter cell at the back. This enables a detailed comparison of electromagnetic and hadronic energy on a tower-by-tower basis. The towers are projective, pointing back to the interaction region, and are 0.1 units wide in η. The tower widths in azimuthal angle are 15° in the central region ($|\eta| < 1.1$ for the EM cells and $|\eta| < 1.3$ for the hadron cells) and 5° at larger $|\eta|$. The EM calorimeter cells are constructed from active sampling layers sandwiched between lead radiator plates. The active layers are scintillators in the central region and gas proportional chambers for $|\eta| \geq 1.1$. In the central region a proportional strip chamber is located at a depth of six radiation lengths, corresponding to the depth of maximum energy deposition in an electromagnetic shower. This enables transverse shower profiles to be measured, and showers to be located with a precision of ±2 mm. The hadron calorimeter cells also use scintillator as the active medium in the central region and gas proportional chambers for $|\eta| \geq 1.3$. In both cases the active layers are sandwiched between iron absorbers. In the central region TDCs record the time at which the energy deposition in the hadron calorimeter cells occurred. This enables rejection of spurious energy depositions which are not in time with the beam-beam crossing. These result from cosmic-ray interactions in the hadron calorimeters. The energy resolution of the EM calorimeter for electrons is given by $\sigma_E/E = 0.135/\sqrt{E_T} \oplus 0.02$ in the central region and $\sigma_E/E = 0.28/\sqrt{E} \oplus 0.02$ at $|\eta| > 1.1$, where the $\oplus$ symbol indicates that the constant term is added in quadrature. The corresponding pion energy resolution of the hadron calorimeter is $\sigma_E/E = 0.75/\sqrt{E} \oplus 0.03$ in the central region and $0.9/\sqrt{E} \oplus 0.04$ at $|\eta| > 1.3$.

C. Muon detection

Muons with p_T in excess of about 2 GeV/c are detected in the central region by four layers of drift chambers located outside of the hadron calorimeters and covering the angular region $56° < \theta < 124°$. Within this angular interval, allowing for the spaces between chambers, the average coverage is 84%. The four layers measure points along the trajectories of particles that penetrate the calorimeters with a precision of 250 μm in the ϕ direction and 1.5 mm in the Z direction.

D. The $\sum E_T$ trigger

Scintillation counters arranged in a rectangle around the beam pipe and covering the angular interval from 0.3° to 4.5° and from 355.5° to 359.7° provide a "minimum bias" trigger, which is satisfied if at least one scintillation counter on each side of the interaction region is above threshold within a 15-ns window centered on the beam-beam crossing time. Events satisfying the minimum-bias trigger are then considered by the higher-

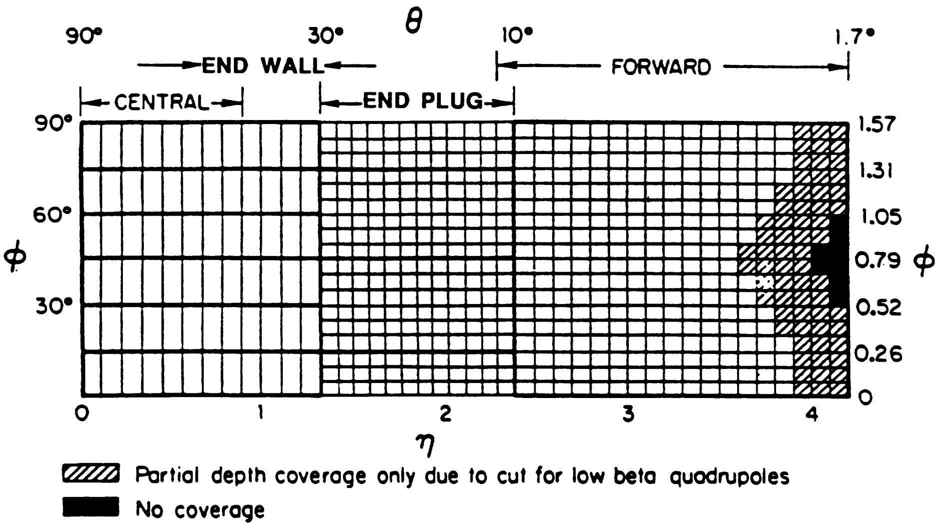

FIG. 2. Calorimeter towers in one of eight identical η-ϕ quadrants ($\Delta\phi = 90°$, $\eta > 0$). The heavy lines indicate module or chamber boundaries.

level trigger logic in CDF.

The $\sum E_T$ trigger exploits the projective geometry of the calorimeter towers. Both hadron and EM calorimeter cells are summed into logical trigger cells with widths $\Delta\eta \approx 0.2$ and $\Delta\phi = 15°$. This results in a representation of the entire detector as a 42×24 matrix in η-ϕ space for both the hadronic and EM calorimeters. Outputs from all phototubes are brought to the counting room individually and summed in groups corresponding to the trigger cells. Outputs from the gas calorimeters are summed into logical trigger towers by the front end electronics. The signals are weighted by $\sin\theta$ to estimate the transverse energy E_T deposited in each trigger cell. The sum over all hadronic and EM trigger cells, each above an E_T threshold of 1 GeV, was used to provide an estimate of the $\sum E_T$ in the event. The high-$\sum E_T$ data sample described in this paper was obtained using one of two triggers: the TOTAL_ET_120 and TOTAL_ET_150 triggers which required $\sum E_T$ in excess of 120 and 150 GeV, respectively. During one-half of the data taking period the TOTAL_ET_120 trigger also required events to have $\sum E_T > 40$ GeV computed on line by a microprocessor farm, where the sum was over individual hadronic and electromagnetic calorimeter cells exceeding an E_T threshold of 1 GeV.

III. JET RECONSTRUCTION

High-$\sum E_T$ events are expected to contain high-p_T hadronic jets which result in localized energy depositions in the CDF calorimeters. Jets are reconstructed using an algorithm which forms clusters from the recorded energies deposited in the calorimeter towers.

The CDF jet algorithm begins by searching for calorimeter towers with $E_T > 1$ GeV. These seed towers are grouped together to form clusters if their separation in η-ϕ space $\Delta R < R_0$, where $\Delta R \equiv (\Delta\eta^2 + \Delta\phi^2)^{1/2}$. The separation $R_0 = 0.7$ is used for the analysis described in this paper. The cluster directions in η-ϕ space are computed from the E_T weighted center of gravities of the constituent tower energy depositions. Additional towers with E_T greater than a threshold E_{T_0} are added to the clusters if their separation $\Delta R < R_0$. In the present analysis E_{T_0} was set equal to 0.5 GeV. The cluster directions are then recomputed and the lists of additional towers are recalculated using the new cluster directions. The process of recomputing the additional tower lists and the resulting cluster directions is repeated until the list of towers associated with each cluster remains unchanged in two consecutive passes. At the end of this process towers can in principle be assigned to more than one cluster. If this happens then the two overlapping clusters are merged if more than 75% of the E_T of the lowest-E_T cluster is in the overlapping region. If this is not the case then the towers in the overlap region are assigned to the nearest cluster in η-ϕ space.

The energy and momentum of each reconstructed jet are computed from the energy depositions in the associated cluster cells:

$$(E_J, p_x^J, p_y^J, p_z^J) = \left[\sum_i^N E_i, \sum_i^N E_i \sin\theta_i \cos\phi_i, \sum_i^N E_i \sin\theta_i \sin\phi_i, \sum_i^N E_i \cos\theta_i \right] .$$

In the present analysis jets have been retained if they have $p_T > 10$ GeV/c and $|\eta| < 2$ unless otherwise stated. Further details about the CDF jet reconstruction algorithm can be found in Ref. [2]. Note that in the analysis presented in the present paper jet energies and momenta have not been corrected for detector effects; uncorrected jet properties are compared with predictions in which the effect of the detector has been taken into account using a simulation of the CDF detector as described in Sec. IV.

IV. MONTE CARLO PREDICTIONS

We would like to know if the rate and detailed properties of the high-$\sum E_T$ events observed by CDF are consistent with QCD expectations. To address this question we compare uncorrected measured distributions with QCD predictions obtained by using the HERWIG [3] event generator (version 4.3) together with a simulation of the CDF detector.

A. The HERWIG Monte Carlo Program

HERWIG is a leading-order parton shower Monte Carlo program that includes both initial- and final-state gluon radiation. Gluon emission is described by successive branchings for which the available phase space is reduced to an angular-ordered region in which the branching angles decrease as one moves away from the hard vertex. Outside of this angular-ordered region the coherence of different emission diagrams leads to destructive interference and to leading order the azimuthally integrated distribution vanishes. Coherence therefore restricts the angular extent of the parton shower. In initial-state radiation, if the radiated gluon carries only a small fraction of its parent's energy, coherence amounts to an ordering in the p_T of the radiated gluons which increases as the hard parton-parton interaction is approached. If a gluon radiated from the initial state carries a large fraction of its parent's energy coherence amounts to an ordering in the angle between the radiated gluon and the incoming initial-state parton, which implies that the cascade retains a memory of the incoming parton direction. For final-state radiation coherence amounts to requiring that the emission angles of the radiated gluons with respect to their parents direction decrease at each branching. In the parton shower the internal legs after the primary parton-parton scattering are timelike, and those before the hard parton-parton scattering are spacelike, the virtuality of the space-like partons increasing as the primary hard vertex is approached.

Gluon radiation is stopped when the virtual gluon mass falls below a cutoff which is set equal to 0.65 GeV/c^2. All outgoing gluons are then split into light (u or d) quark-antiquark pairs with an isotropic distribution in the gluon rest frame, where the virtual-gluon mass is set equal to the cutoff value. The quarks and antiquarks are then combined into color-singlet clusters by taking a quark from one gluon with an antiquark from a neighboring gluon. The distribution of cluster masses peaks at low values. There are a small number of clusters that have high mass and these are forced to undergo fission until their mass falls below a fission threshold of 3 GeV/c^2. Clusters with a mass less than the fission threshold but greater than twice the mass of the lightest available hadron are decayed isotropically into pairs of hadrons. Clusters too light to decay into a hadron pair are identified with the lightest available hadron where the mass shift is accommodated by exchange of energy with a neighboring cluster. This fragmentation model conserves energy, momentum, and flavor.

The HERWIG Monte Carlo program treats the spectator system as a soft collision between beam clusters, using a parametrization based on UA5 data from the CERN $p\bar{p}$ Collider, followed by the same fragmentation model used for the hard parton-parton scattering. The spectator system is treated independently of the hard parton-parton scattering.

HERWIG generates 2→2 processes above a specified p_T^{hard}, where p_T^{hard} is the p_T of the outgoing partons from the hard scatter before any radiation has occurred. We have set the minimum p_T^{hard} to 80 GeV/c. This relatively low value of p_T^{hard} is necessary to obtain an unbiased Monte Carlo sample in which adequate account is taken of events in which the detector response has fluctuated upwards by several standard deviations and/or the spectator system, including the initial-state radiation, makes an unusually large contribution to the $\sum E_T$. The contribution to the $\sum E_T > 400$ GeV sample from events with an underlying $p_T^{\text{hard}} < 80$ GeV/c is estimated to be less than 1%. Unfortunately with a minimum p_T^{hard} of 80 GeV/c many events must be generated to obtain one event with an observed $\sum E_T > 400$ GeV and the statistical significance of the Monte Carlo samples is therefore limited by the availability of computing resources.

B. Simulation of the CDF detector

The observed energy depositions in the detector are on average less than the true energies of the associated particles for a variety of reasons: (i) the calorimeter response to low-energy charged pions is nonlinear, (ii) the radius of curvature of charged particles with $p_T < 400$ MeV/c in the CDF magnetic field is such that they do not reach the calorimeter, (iii) the energy of particles showering in uninstrumented regions of the calorimeter is fully or partially lost (for example at the ϕ boundaries between calorimeter modules in the central region, or at the η boundaries between the two halves of the central calorimeter), and (iv) energy taken away by neutrinos is not detected in the calorimeter, and only a small fraction of the energy of muons with $p_T \gg 2$ GeV/c is detected. As a result of these effects the $\sum E_T$ detected in an event tends to be less than the sum of the transverse energies of the outgoing stable particles produced in the interaction. The calculated ratio of detected to generated $\sum E_T$ is shown as a function of the generated $\sum E_T$ in Fig. 3, which was obtained using the HERWIG Monte Carlo generator together with the CDF detector simulation program. At high $\sum E_T$ most of the E_T loss is due to energy deposited in uninstrumented regions of the calorimeters. On average about 80% of the generated E_T is detected. At lower $\sum E_T$ the relative losses due to the calorimeter nonlinearities and the low-p_T cutoff imposed by the magnetic field become more important, and the fraction of the generated E_T that is detected decreases with decreasing $\sum E_T$. In the region of interest (observed $\sum E_T > 400$ GeV) most of the observed E_T is associated with high-p_T jet production, and to a good approximation the measured jet-p_T's, as well as the measured $\sum E_T$, are expected on average to be about 80% of the sum of the transverse momenta of the particles associated with the jet. Further details of the relationship between generated and reconstructed jet parameters can be found in Ref. [2].

In the analysis described in this paper measured distributions are compared with QCD predictions based on the HERWIG Monte Carlo program and a simulation of the CDF detector. The detector simulation program extrapolates the final-state particle trajectories through the magnetic field to the calorimeter cells. The average calorimeter responses and resolutions for charged pions, photons, electrons, and muons have been parametrized and tuned to reproduce (i) test-beam measurements for particles with momenta from a few GeV/c up to about 200 GeV/c, and (ii) studies of isolated charged particles produced in proton-antiproton collisions. The simulation includes the variation of response across boundaries between calorimeter cells, zero response in uninstrumented regions, calorimeter nonlinearities, and the observed dis-

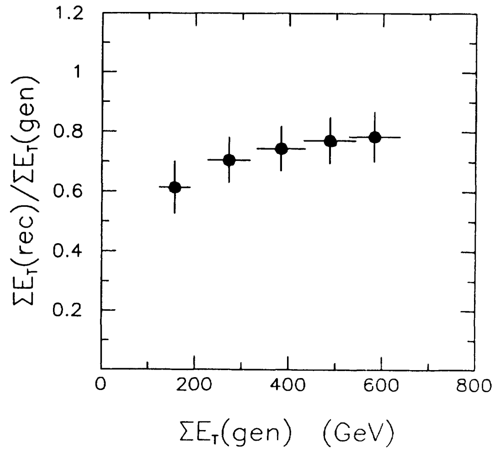

FIG. 3. The calculated ratio of detected to generated $\sum E_T$ shown as a function of the generated $\sum E_T$ for five HERWIG Monte Carlo event samples corresponding to five different ranges of generated p_T^{hard}. The horizontal "error bars" indicate the rms of the generated $\sum E_T$ distributions corresponding to each generated p_T^{hard} range. The CDF detector simulation was used to calculate the detected $\sum E_T$ for each Monte Carlo event.

tribution of vertex positions about the mean position at the center of the detector.

C. Systematic uncertainties

Uncertainties on the QCD predictions arise from uncertainties on the choice of structure function for the colliding hadrons, the Q^2 scale used in evaluating the running strong coupling constant $\alpha_s(Q^2)$ for the hard parton-parton scattering, and the fragmentation model used for the outgoing hadron jets. In addition there is an uncertainty on the simulation of the detector response.

The structure functions available in HERWIG version 4.3 are Duke-Owens [4] sets 1 and 2 (DO1, DO2), Eichten-Hinchliffe-Lane-Quigg [5] sets 1 and 2 (EHLQ1, EHLQ2). Both DO and EHLQ have $\Lambda_{\mathrm{QCD}}=200$ GeV for set 1 and $\Lambda_{\mathrm{QCD}}=400$ GeV for set 2. To map out the variation in the predictions with choice of structure function, Monte Carlo data sets have been generated for all four structure-function sets. Note that more modern structure functions which have recently become available tend to yield predictions within the envelope bracketed by the DO and EHLQ structure functions. The Q^2 scale for the hard interaction is defined in HERWIG as

$$Q^2=\frac{2stu}{s^2+t^2+u^2} ,$$

where s, t, and u are the Mandelstam variables. This scale is approximately equal to $(p_T^{\mathrm{hard}})^2$. To map out the variation in the predictions with choice of the Q^2 scale we have also generated Monte Carlo data sets with $Q^2=stu/2(s^2+t^2+u^2)$ and $Q^2=8stu/(s^2+t^2+u^2)$. To estimate the uncertainties associated with the fragmentation model used in HERWIG, in addition to generating data states using HERWIG version 4.3, we have also generated a Monte Carlo data set using version 5.0 in which the parameters controlling the fragmentation have been retuned on OPAL data. In particular the virtual-gluon mass cutoff has been increased to 0.75 GeV/c^2, and the fission threshold has been raised to 3.5 GeV/c^2. To account for the uncertainties in the calorimeter response implemented in the detector simulation program, Monte Carlo data sets were generated with the nominal calorimeter response increased by one standard deviation and decreased by one standard deviation.

There are thus a total of nine HERWIG Monte Carlo samples, which are listed in Table I, that have been reconstructed using the CDF detector simulation and reconstruction code. Each Monte Carlo sample has been generated so that it contains about 500 events after application of the event-selection criteria used to select high-$\sum E_T$ events from the CDF data.

V. EVENT SELECTION

The highest $\sum E_T$ events have been selected from the TOTAL_ET_120 and TOTAL_ET_150 triggers described in Sec. II D. These events were passed through a prefilter that required $\sum E_T > 45$ GeV, where the sum was over all clusters with $E_T > 5$ GeV.

The primary selection criterion for the high-$\sum E_T$ event sample was the requirement $\sum E_T > 400$ GeV. In the present analysis the sum is over all calorimeter towers with $E_T \geq 500$ MeV. The 500-MeV threshold was chosen to (i) be high enough to ensure that any differences observed between data and Monte Carlo predictions are not due to poor simulation of noise in the calorimeters, (ii) reduce to an acceptable level the contamination from multiple-interaction events which is observed to decrease as the calorimeter tower threshold is raised, and (iii) be low enough such that we do not seriously bias our sample against nonjetlike events having high $\sum E_T$. Large pulses are sometimes observed in isolated gas proportional chamber sampling layers of the calorimeter towers covering the region $|\eta| > 1$. These pulses are believed to be due to neutron interactions [6] in the chambers, and are removed on an event-by-event basis before the $\sum E_T$ is calculated.

The requirement $\sum E_T > 400$ GeV selects 1189 events. The high $\sum E_T$ in many of these events can be attributed to a high-energy cosmic-ray interaction in one of the calorimeters, or a large energy deposition associated with one or more beam halo particles interacting in the gas calorimeters. To reduce these backgrounds we reject events with a total observed energy in excess of 2000 GeV, or with a large energy deposition in the central hadron calorimeter out of time with the proton-antiproton collision. We are left with 358 events.

The remaining cosmic-ray and beam halo background is expected to exhibit a large transverse-energy imbalance. We define the missing-transverse-energy significance [7]

$$S \equiv \not{E}_T \Big/ \left[\sum E_T\right]^{1/2} ,$$

TABLE I. Summary of Monte Carlo event samples.

HERWIG version	Structure function	Q^2 scale	Calorimeter response
4.3	DO1	$2stu/(s^2+t^2+u^2)$	Nominal
4.3	DO2	$2stu/(s^2+t^2+u^2)$	Nominal
4.3	EHLQ1	$2stu/(s^2+t^2+u^2)$	Nominal
4.3	EHLQ2	$2stu/(s^2+t^2+u^2)$	Nominal
4.3	DO1	$stu/2(s^2+t^2+u^2)$	Nominal
4.3	DO1	$8stu/(s^2+t^2+u^2)$	Nominal
4.3	DO1	$2stu/(s^2+t^2+u^2)$	$+1\sigma$
4.3	DO1	$2stu/(s^2+t^2+u^2)$	-1σ
5.0	DO1	$2stu/(s^2+t^2+u^2)$	Nominal

where the missing-transverse-energy

$$\not{E}_T \equiv \left| \sum_i \bar{E}_{T_i} \right| ,$$

and $\bar{E}_{T_i}$ is a vector which points from the interaction point to the calorimeter cell and has a magnitude equal to the cell E_T. The distribution of S for the high-$\sum E_T$ event sample is compared in Fig. 4 with the expectations from the HERWIG Monte Carlo plus CDF detector simulation Monte Carlo program. The distribution of events at low S is well described by the Monte Carlo program. However, in the region $S > 6$ where we predict only two events we observe 51 events. The fraction of the $\sum E_T$ deposited in the EM calorimeters is shown in Fig. 5 for (a) the 51 events with $S > 6$, and (b) the 307 events with $S < 6$. The majority of the high-S events have an EM fraction close to zero or one, characteristic of cosmic-ray and beam halo interactions. We therefore remove the high-S events from our sample by requiring that $S < 6$. To confirm that the rejected high-S events are due to cosmic-ray or beam halo interactions they were inspected using a high-resolution graphics display. This revealed that (a) five events have large $\sum E_T$ and large $\not{E}_T$ due to beam halo interactions in the gas calorimeters, (b) 45 events have large $\sum E_T$ and large $\not{E}_T$ due to well-identified cosmic rays that deposited energy in the central calorimeters [among these cosmic-ray events are the two events in Fig. 5(a) with EM fraction between 0.1 and 0.9; these events have S values of 17 and 26], and (c) 1 event has a large $\sum E_T$ and large $\not{E}_T$ due to an isolated neutral energy deposition in the central EM calorimeters. Although we are unable to unambiguously identify this last event as a cosmic-ray interaction its characteristics are consistent with this hypothesis. Thus all 51 rejected high-S events are beam halo events or well identified or suspected cosmic-ray interactions.

The $\not{E}_T$ distribution for the surviving 307 high-$\sum E_T$ events is shown in Fig. 6 to be well described by our expectations based on HERWIG and the CDF detector simulation. The predicted $\not{E}_T$ distribution reflects the experimental resolution on the measurement of the $\not{E}_T$. There is no evidence for a significant contribution to the high-$\sum E_T$ event sample from events in which high-p_T neutrinos or other noninteracting particles are emitted.

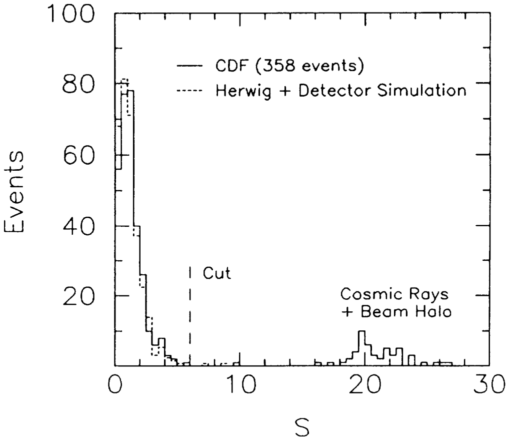

FIG. 4. The distribution of missing-E_T significance (S) for high-$\sum E_T$ events before the S cut (solid histogram, see Sec. V) compared with the expectation for QCD jet events based on the CDF detector simulation program (broken histogram). Note that a spurious energy deposition of 400 GeV would appear at $S=20$ if there were no other energy depositions in the "event."

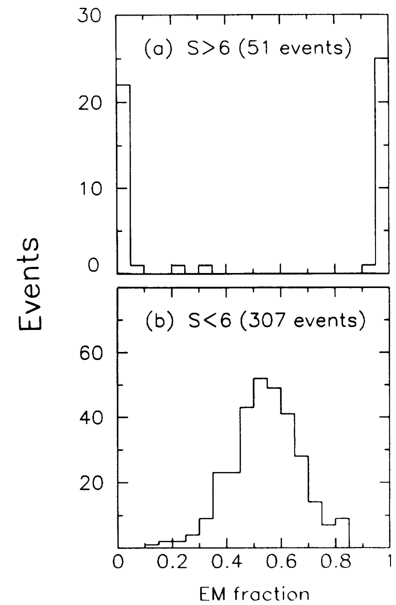

FIG. 5. The fraction of the observed $\sum E_T$ in the electromagnetic calorimeters for those high-$\sum E_T$ events with (a) $S > 6$, and (b) $S < 6$.

Finally, we wish to minimize the contribution to the event sample from multiple interactions in which the high-$\sum E_T$ is due to the combined contributions from two or more events. Note that a high-$\sum E_T$ trigger of the type we have used to obtain our event sample is biased towards multiple interactions. A check was therefore made for a second interaction reconstructed in the VTPC. In order to unambiguously define a second vertex we require at least 10 associated VTPC tracks for both vertices and a

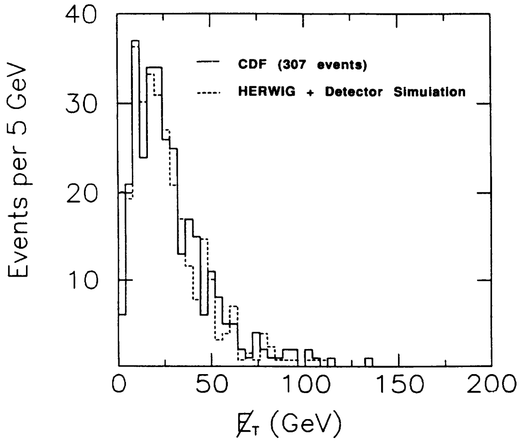

FIG. 6. Missing-transverse-energy distribution for events with $\sum E_T > 400$ GeV and $S < 6$ (solid histogram) compared with expectations based on HERWIG and the CDF detector simulation (dashed histogram).

two-vertex separation in excess of 10 cm. In the sample passing the preceding cuts there are 28 events with at least two vertices reconstructed in the VTPC each with ≥ 10 associated tracks and a two-vertex separation > 10 cm. We classify these as resolved multiple interactions and remove them from our sample. The final high-$\sum E_T$ sample consists of 279 events.

VI. MULTIPLE INTERACTIONS

Although the selection procedure removes events containing more than one identified $p\bar{p}$ interaction, multiple interactions not resolved in the VTPC remain in the sample. To calculate the contribution from unresolved multiple interactions to the high-$\sum E_T$ event sample we begin by defining the quantities N_n $(n=1,2,3,\dots)$ which specify the total number of beam-beam crossings containing n $p\bar{p}$ interactions in a minimum-bias event sample. Using the luminosity history corresponding to the high-$\sum E_T$ sample together with the minimum-bias trigger cross section of 41 mb we obtain $N_1=1.8\times10^{11}$, $N_2=1.2\times10^{10}$, and $N_3=6.1\times10^{8}$. Therefore, the ratio of double interactions to single interactions in minimum-bias events in $N_2/N_1=0.068$. To compute the fraction of events containing multiple interactions in the high-$\sum E_T$ sample we extract the $\sum E_T$ spectrum of the multiple interactions from the observed $\sum E_T$ spectrum (Fig. 7), which contains contributions from both single and multiple interactions. This calculation can be done either analytically or by an event mixing technique. Both methods have been used and give similar results. The event mixing technique enables the cuts applied in the $\sum E_T$ selection to be taken into account, and the expected properties of multiple interactions contributing to the high-$\sum E_T$ sample to be calculated. Figure 8(a) shows as a function of $\sum E_T$ the predicted and observed fractions of events containing a multiple interaction that was resolved in the VTPC (vertex separation > 10 cm, and ≥ 10 tracks associated to each vertex). Small differences between the predictions of the event mixing and analytical techniques are due to vertex assignment and single tower threshold effects in the calculation of the $\sum E_T$ for double interactions. These small effects are not included in the analytical calculation which assumes that the $\sum E_T$ contributions from the two component events add linearly. The predictions give a reasonable description of the data at high $\sum E_T$, and demonstrate our ability to predict multiple-interaction rates. In particular we predict that there should be 22±2 resolved multiple interactions removed by the VTPC cuts, in agreement with the 28 events actually removed. In Fig. 8(b) the predicted fraction of events containing multiple interactions is shown as a function of $\sum E_T$ for multiple interactions not resolved in the VTPC. At high $\sum E_T$ the predicted fraction is 5.0±0.5%, where the quoted uncertainty takes into account systematic uncertainties arising from the uncertainties on luminosity variations between different proton and antiproton bunches and variations over individual data runs, uncertainties on the observed $\sum E_T$ spectrum due to trigger biases, and uncertainties on the uncalculated contributions from multiple interactions with $n > 3$.

In the sample of 279 events with $\sum E_T > 400$ GeV we expect 14±1 events containing an unresolved second interaction. The event mixing calculation predicts that the contribution to the $\sum E_T$ from the second interactions in these events is only 1.3% on average, and that the 14 second interactions in the sample contribute a total of less than one jet with $p_T > 10$ GeV/c. The contributions to the high-$\sum E_T$ event sample from multiple interactions can therefore be neglected.

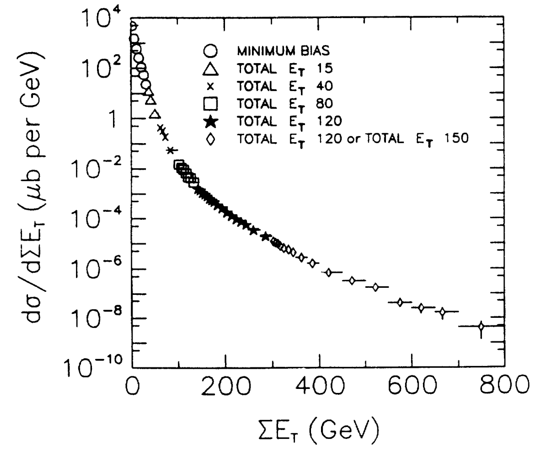

FIG. 7. The observed raw $\sum E_T$ distribution assembled from a minimum-bias trigger and a variety of high-$\sum E_T$ triggers (as indicated). The $\sum E_T$ has been computed with a single tower threshold of 500 MeV.

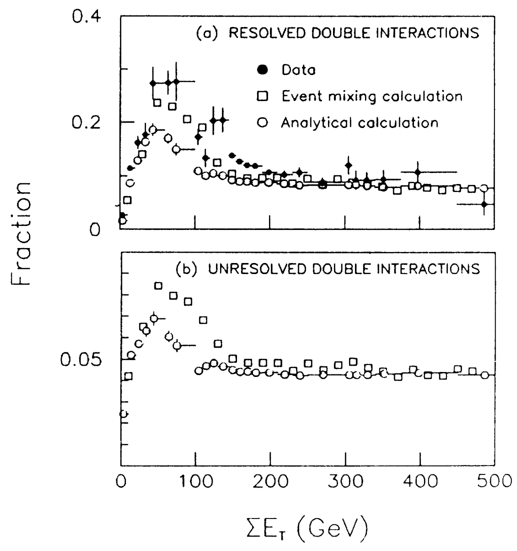

FIG. 8. The predicted fraction of events containing (a) resolved double interactions in the VTPC ($N_{\mathrm{trk}} \geq 10, \Delta Z > 10$ cm), and (b) unresolved double interactions, shown as a function of $\sum E_T$. The predictions have been obtained using the analytical (open circles) and event mixing (open squares) calculations described in the text. The resolved double interaction fraction is compared with the observed second vertex rate in the VTPC (solid circles).

VII. EVENT CHARACTERISTICS AND THE SEARCH FOR HIGH-P_T LEPTONS AND PHOTONS

The 279 events in the final high-$\sum E_T$ sample were inspected on a graphics display, and all were found to have significant high-p_T jet activity. Most events have a well-defined two-jet or three-jet topology. All events have a well-defined vertex in the VTPC. The energy flow in the plane transverse to the beam axis is shown in Figs. 9(a), 9(b), and 9(c) for the three events with the highest $\sum E_T$'s. Some events in the sample have a more complicated multijet topology. A particularly striking example is shown in Fig. 9(d).

A search was made for isolated central electrons and photons in the high-$\sum E_T$ events by selecting clusters in the central EM calorimeter passing the following requirements: (i) $p_T > 10$ GeV/c, (ii) $|\eta| < 1$, (iii) $E_{\text{had}}/E_{\text{EM}} < 0.1$ where E_{EM} and E_{had} are, respectively, the EM cluster energy and the energy in the hadronic calorimeter cells immediately behind the EM cluster, (iv) $E_T^{\text{border}} < 0.1 E_T^{\text{EM}}$ where E_T^{EM} is the EM cluster E_T and E_T^{border} is the sum of the transverse energies in the calorimeter cells adjacent to the EM cluster towers, and (v) the number of CTC tracks pointing to the cluster $N_{\text{trk}} = 0$ or 1 for photon and electron candidates, respectively, and for electron candidates the track must have a momentum exceeding 10% of the cluster energy. These cuts select three events containing isolated electron candidates and five events containing isolated photon candidates. These events and their properties are listed in Table II.

We interpret the eight events containing electron or photon candidates as follows.

(a) Photon + jet(s) events. The observed rate of photon + jet(s) events is consistent with our expectations for (i) jet fluctuations that fake isolated high-p_T photons (0.9 ± 0.2 fake photons) which we estimate by applying our selection criteria to the Monte Carlo high-$\sum E_T$ sample generated using HERWIG and a simulation of the CDF detector, and (ii) direct photon production (1.2 ± 0.1 direct photons) which we estimate using the HERWIG Monte Carlo program and a simulation of the CDF detector to generate photon + jet events to $O(\alpha\alpha_s)$.

(b) Diphoton event [Fig. 10(a)]. Using the HERWIG Monte Carlo program and the CDF detector simulation program we predict that one in six hundred jets in the high-$\sum E_T$ sample with $E_T > 10$ GeV and $|\eta| < 1$ fluctuate such that they pass the isolated photon selection criteria. Taking into account the additional jet activity observed in the five events containing at least one photon candidate, we estimate that we expect 0.02 diphoton candidates in our event sample from this process. In addition we expect a contribution from QCD production of events with two photons, which we estimate is less than or of order 0.1 events.

(c) (e + jet) and (e + jets) events. The observed rate of e + jet(s) events is consistent with our expectations for (i) jet fluctuations and heavy flavor production and decay giving genuine or fake isolated electron candidates (0.5 ± 0.2 events) which we estimate by applying our selection criteria to the Monte Carlo high-$\sum E_T$ sample generated using the HERWIG Monte Carlo program and a simulation of the CDF detector, and (ii) W-boson production and decay (0.8 ± 0.4 events) which we also estimate by applying our selection criteria to a HERWIG Monte Carlo sample after detector simulation.

(d) (e^+e^- + jet) event [Fig. 10(b)]: The e^+e^- pair mass is 88 GeV/c^2. We interpret this event as the production and (e^+e^-) decay of a high-p_T Z^0 boson [8].

To search for central isolated high-p_T muons and hadronic one-prong τ-lepton decays in the high-$\sum E_T$ event

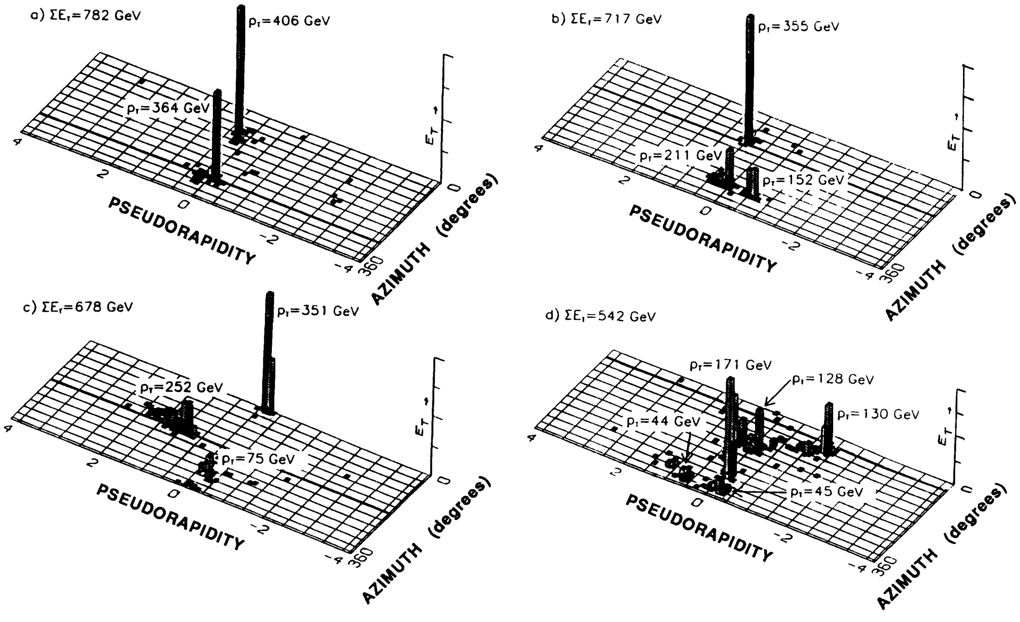

FIG. 9. Energy flow in the transverse plane for the three events containing the highest total transverse energies [(a)–(c)] observed in the CDF high-$\sum E_T$ data sample, and (d) an example of an event with a complicated jet topology.

sample, and to confirm the results of the search for central isolated high-p_T electrons, we have selected CTC tracks with $P_T > 10$ GeV/c and $|\eta| < 1$ passing the following quality and isolation cuts: (i) impact-parameter cut $|D| < 0.5$ cm where $|D|$ is the distance of the extrapolated track trajectory from the beam axis at the point of closest approach, (ii) distance of track extrapolation from the vertex in the Z direction $|\Delta Z|/\sigma_Z < 4$, (iii) $\sum p_T < 2$ GeV/c summed over all additional CTC tracks in a cone centered on the track direction and of radius $\Delta R = 0.4$, and (iv) $\sum p_T < 5$ GeV/c summed over all additional CTC tracks in an annulus with inner radius $\Delta R = 0.4$ and outer radius $\Delta R = 0.7$. Only three tracks in the sample pass these requirements, of which two are the e^+ and e^- in the high-p_T Z^0 event, and one is the electron in the (e + jet) event. The electron in the (e + 3 jets) event did not pass the selection because it failed cut (iv), the nearest jet being within $\Delta R = 0.7$ of the electron candidate. Thus there are no central isolated high-p_T muon candidates in the sample; the only central isolated high-p_T electron candidates are those listed in Table II, and there are no isolated one-prong hadronic τ-lepton decay candidates in the sample. It should be noted that energetic muons or τ leptons deposit only a part of their energy in the calorimeters. More events containing high-p_T electrons are therefore expected in the high-$\sum E_T$ event sample than those containing high-p_T τ leptons or muons.

VIII. THE $d\sigma/d\sum E_T$ DISTRIBUTION

The uncorrected $\sum E_T$ spectrum for the high-$\sum E_T$ event sample is compared in Fig. 11 with the leading-order QCD expectations using the DO1 structure functions and $Q^2 = stu/2(s^2+t^2+u^2)$. The best description of the data for this choice of structure functions and Q^2 scale ($\chi^2 = 12.3$ for 10 degrees of freedom) is obtained when the predictions are scaled upwards by a factor $K = 1.12$. The QCD prediction for the shape of the differential cross section tends to fall more steeply than the data, but is within the band of systematic experimental uncertainty associated with the uncertainty in the calorimeter energy scale. The other choices of structure function and Q^2 scale we have used give similar predictions for the shape of the $\sum E_T$ spectrum, indistinguishable within the statistical uncertainty on the calculations,

TABLE II. Properties of the eight events containing electron or photon candidates in the $\sum E_T > 400$ GeV sample. The electron and photon candidates pass the requirements: (i) $E_T > 10$ GeV, (ii) $|\eta| < 1$, (iii) $E_{\text{had}}/E_{\text{EM}} < 0.1$, (iv) E_T in the towers bordering the EM cluster $< 0.1\ E_T^{\text{EM}}$. In addition the photons are required to have no CTC tracks associated with the cluster, and the electrons to have one and only one track associated with the cluster and this track must have a momentum exceeding 10% of the cluster energy.

Events			Clusters					
Type	$\sum E_T$ (GeV)	s[a]	Type	E (GeV)	p_T (GeV/c)	ϕ (deg)	η	Comments
γ+jet	434	2.1	γ	285	234	82	-0.65	
			jet	199	190	256	0.23	
γ+jets	470	1.3	γ	206	196	180	-0.33	
			jet	189	186	339	-0.06	
			jet	257	72	87	1.95	
γ+jets	516	4.6	γ	293	293	333	-0.03	
			jet	113	109	163	-0.21	
			jet	97	88	135	-0.40	
γ+jets	520	1.7	γ	85	78	327	0.44	
			jet	273	272	170	-0.07	
			jet	184	147	2	0.69	
			jet	45	20	321	1.47	
$\gamma\gamma$+jets	524	2.2	γ	189	185	302	-0.21	$m_{\gamma\gamma} = 176$ GeV/c^2
			γ	99	94	25	-0.34	[see Fig. 10(a)]
			jet	176	173	150	0.05	
			jet	37	27	250	0.85	
			jet	42	11	41	1.98	
e+jet	479	3.3	e	356	258	64	0.85	Track $p_T = 64$ GeV/c
			jet	235	201	246	0.57	
e+jets	486	0.5	e	113	87	228	0.76	Track $p_T = 72$ GeV/c
			jet	250	210	59	-0.60	
			jet	115	112	209	0.21	
			jet	81	71	302	0.51	
e^+e^-+jets	427	1.9	e^+	162	121	250	-0.80	$p_T(e^+) = 81$ GeV/c
			e^-	98	97	229	-0.09	$p_T(e^-) = 57$ GeV/c
			jet	184	165	72	-0.43	$p_T(e^+e^-) = 210$ GeV/c
			jet	21	18	13	0.53	$m_{ee} = 88$ GeV/c^2 [see Fig. 10(b)]

[a] The missing E_T significance, $S \equiv \not{E}_T/\sqrt{\sum E_T}$.

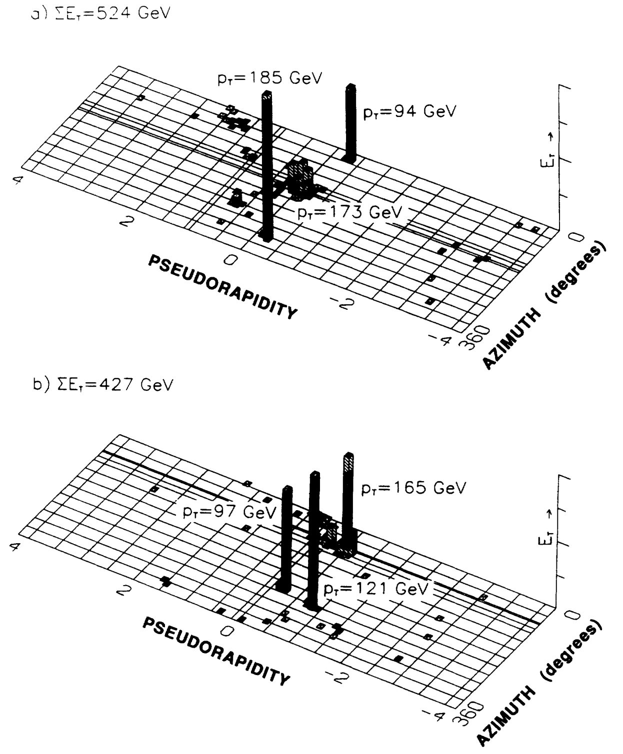

FIG. 10. Energy flow in the transverse plane for (a) the $\gamma\gamma$ +jets candidate event, and (b) the e^+e^- + jets candidate event.

and yield renormalization factors K ranging from 1.5 for DO1, DO2, and EHLQ1 with $Q^2=2stu/(s^2+t^2+u^2)$, to $K=2.8$ for DO1 with $Q^2=8stu/(s^2+t^2+u^2)$. We conclude that there is satisfactory agreement between QCD expectations and the observed $\sum E_T$ spectrum of the highest-$\sum E_T$ events observed by CDF. The data do not distinguish between the various choices of structure function and Q^2 scale we have used.

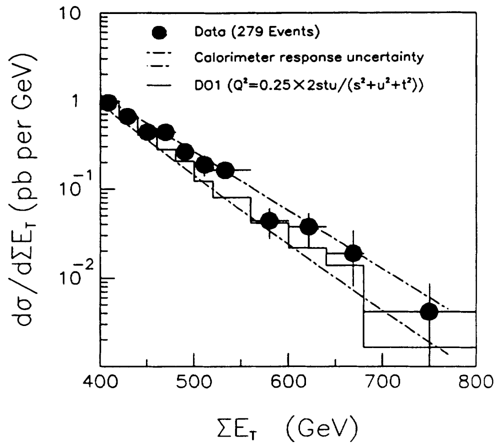

FIG. 11. The observed (uncorrected) $\sum E_T$ distribution in the region $\sum E_T > 400$ GeV (points) compared with the QCD (HERWIG 4.3) Monte Carlo predictions using the DO1 structure functions and $Q^2=stu/2(s^2+t^2+u^2)$. The dot-dashed lines indicate the systematic uncertainty on the measurements associated with the uncertainty on the calorimeter energy scale.

IX. INCLUSIVE JET RATES

In Fig. 12 the observed jet-p_T distribution for the high-$\sum E_T$ event sample is compared with the QCD expectations using the DO and EHLQ structure functions. The distribution shows the expected peaking at 200 GeV/c corresponding to half of the $\sum E_T$ threshold, and an increase in rate as the jet-p_T decreases towards zero. The predictions give a reasonable description of the data, although there is some indication that the observed rate at intermediate jet transverse momenta around 100 GeV/c is lower than the predicted rate. In addition to the differences in the predicted spectra corresponding to different choices of structure function, we have also examined the dependence of the predicted spectrum on fragmentation model differences between HERWIG 4.3 and HERWIG 5.0, and on the experimental uncertainty in the calorimeter response. The resulting differences in the predicted spectra are comparable with the statistical uncertainty of the predictions.

In Fig. 13 the measured jet η distribution are compared with predictions as a function of jet-p_T. As the jet-p_T increases the pseudorapidity "plateau" is seen to shrink. This trend has been observed before at CDF [9] and at the CERN $p\bar{p}$ collider [10]. The variations in the HERWIG predictions for the various choices of structure functions, Q^2 scale, calorimeter response, and HERWIG version are comparable to the statistical uncertainties of the Monte Carlo calculations. The QCD predictions give a reasonable description of the observed η distributions and the shrinking of the pseudorapidity plateau with increasing jet-p_T.

X. SINGLE-JET SHAPES AND MASSES

To see if there is an excess of "fat" jets or "thin" jets in the high-$\sum E_T$ sample, or jets with abnormally high or low mass, we begin by looking at the average jet profiles

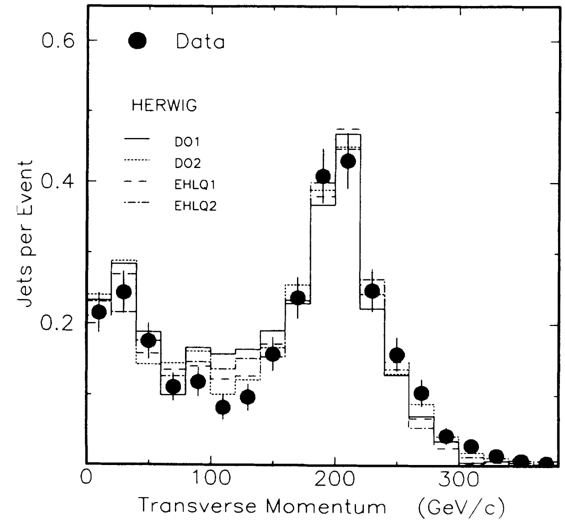

FIG. 12. Jet transverse-momentum distribution for jets with pseudorapidity $|\eta| < 2.0$. The data (points) are compared with HERWIG predictions (histograms) using the structure functions as indicated, and the scale $Q^2=2stu/(s^2+t^2+u^2)$.

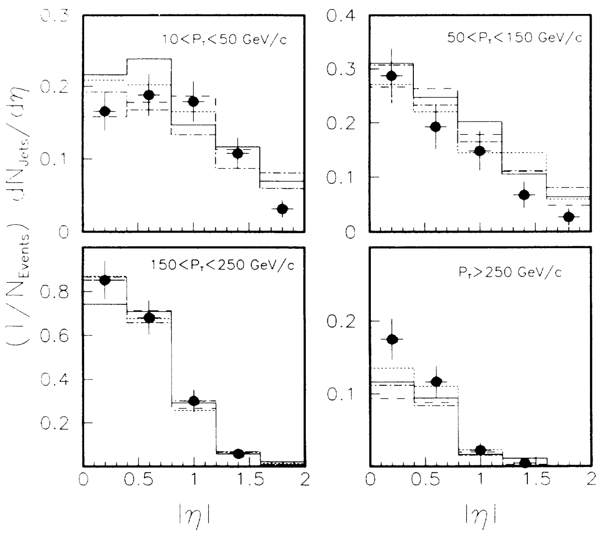

FIG. 13. Jet pseudorapidity distributions shown for four different jet transverse-momentum intervals as indicated. The data (points) are compared with HERWIG predictions using the DO1 (solid line), DO2 (short dashed line), EHLQ1 (long dashed line), and EHLQ2 (dot-dashed line) structure functions, and the scale $Q^2=2stu/(s^2+t^2+u^2)$.

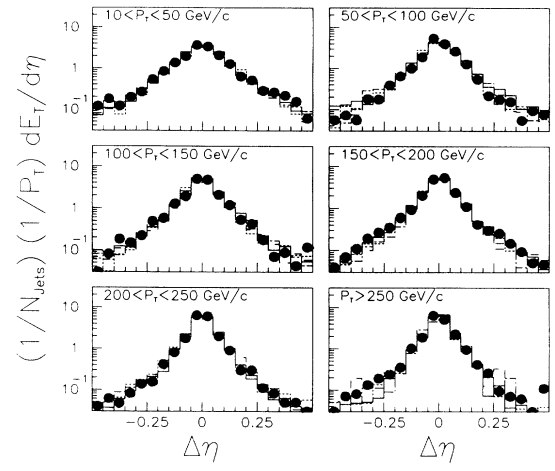

FIG. 14. Average jet profile in pseudorapidity space. The distribution of jet transverse-energy flow is shown for the energy detected within $\Delta\eta<0.5$ and $\Delta\phi<0.5$ of the reconstructed jet axis, averaged over all the jets in the $\sum E_T>400$ GeV sample within the pseudorapidity range $|\Delta\eta|<2.0$, and the p_T range indicated on each of the six plots. The data (points) are compared with four Monte Carlo predictions corresponding to samples generated with HERWIG and each having about twice the statistics of the data.

within a window in η-ϕ space about the reconstructed jet axes. The average jet η profiles have been constructed using all calorimeter cells i with $E_{T_i}>0.5$ GeV that are within $|\Delta\eta_i|<0.5$ and $|\Delta\phi_i|<0.5$ with respect to the jet axis. Each of these cells makes a contribution of magnitude E_{T_i}/p_T to the η profile at position $\Delta\eta$; where p_T is the transverse momentum of the associated jet. This procedure removes the jet-p_T scale from the profile plots. The average jet η profiles are shown in Fig. 14 as a function of the jet-p_T. The widths of the jet profiles shrink as the jet-p_T increases. We note that the calorimeter cell size in the central region is $\Delta\eta=0.1$ and $\Delta\phi=0.26$, and thus the average high-p_T jet in the sample has a core which is comparable to the size of a single cell. Superimposed on the measured jet profiles are four QCD curves, each of which have been calculated from a HERWIG Monte Carlo sample corresponding to twice the statistical significance of the data. Variations between the curves therefore indicate the statistical uncertainty on the measured profiles. The agreement between the observed average jet profiles and the predictions is within this statistical uncertainty, and is impressive. The average jet profiles and their observed shrinking with increasing jet-p_T therefore well described by the fragmentation model implemented in HERWIG. The predicted jet profiles are not sensitive to choice of structure function, Q^2 scale, calorimeter response, or HERWIG version.

We next define the jet η widths:

$$W_\eta \equiv \frac{\sum_i E_{T_i}|\Delta\eta_i|}{\sum_i E_{T_i}} ,$$

where the sums are over all calorimeter towers with transverse energy $E_{T_i}>0.5$ GeV that are within the window ($|\Delta\eta_i|<0.5$, $|\Delta\phi_i|<0.5$) centered on the jet axis. Defined in this way the jet widths are sensitive to the fluctuations of the distribution of energy within the jet profile plots. The observed distributions of W_η are compared with QCD expectations in Fig. 15 as a function of jet-p_T. The predictions, which are not sensitive to choice of structure function, Q^2 scale, calorimeter response, or HERWIG version, give an excellent description of the W_η distributions. Note that the majority of jets with $p_T>50$ GeV/c have $W_\eta<0.1$, and their widths reflect the granularity of the detector and not the intrinsic distribution of hadronic jet widths. A comparison of the W_η distribution for Monte Carlo jets before and after simulation of the detector reveals that the width distribution in the region $W_\eta>0.1$ is not seriously distorted by detector effects. We conclude that there is no evidence for an excess of very fat jets with $W_\eta>0.1$.

Another measure of jet width is the single-jet mass M_J which we construct from the energy vectors $\bar{E}_i$, defined as the vectors which have length equal to the calorimeter tower energies E_i and point from the interaction vertex to the center of the calorimeter cells. The single-jet mass is then defined such that

$$M_J^2 \equiv \left[\sum_i E_i\right]^2 - \sum_i (\bar{E}_i)^2 ,$$

where the sums are over all calorimeter towers having $E_{T_i}>0.5$ GeV within the window ($|\Delta\eta_i|<0.5$, $|\Delta\phi_i|<0.5$) centered on the reconstructed jet axis. The single-jet mass distributions are compared to the Monte Carlo predictions in Fig. 16 as a function of jet-p_T. The average jet mass is seen to increase with p_T. The predic-

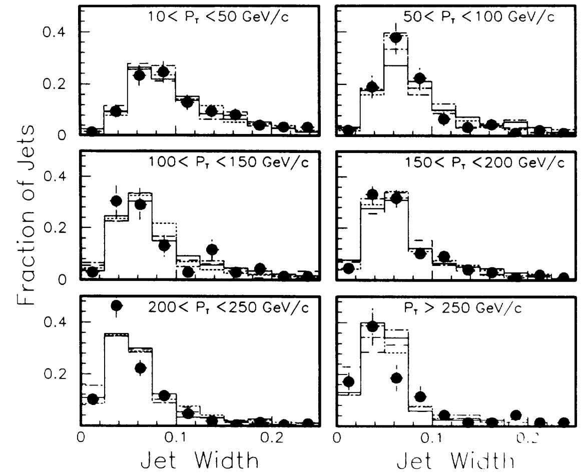

FIG. 15. Distribution of jet widths in pseudorapidity space W_η (as defined in the text) shown for six different regions of jet transverse momenta as indicated. The data (points) are compared with HERWIG predictions using the DO1 (solid line), DO2 (short dashed line), EHLQ1 (long dashed line), and EHLQ2 (dot-dashed line) structure functions, and the scale $Q^2=2stu/(s^2+t^2+u^2)$.

tions give a good description of the data. A comparison of the M_J distribution for Monte Carlo–generated jets before and after simulation of the detector reveals that the reconstructed M_J distribution for jets with low observed p_T ($p_T<100$ GeV/c) peaks at significantly lower masses than the corresponding distribution calculated from the generated particle four-momenta associated with the cluster. This reflects the detector effects described in Sec. IV B and the finite granularity of the calorimeters. The M_J distribution is also seen to be distorted by detector effects for higher p_T jets in the low M_J region. However, for Monte Carlo–generated jets with $p_T>100$ GeV/c the reconstructed single-jet mass distribution in the region $M_J>20$ GeV/c^2 is not significantly changed by the detector simulation. We conclude that there is no evidence for an excess of very massive jets with $p_T>100$ GeV/c and $M_J>20$ GeV/c^2.

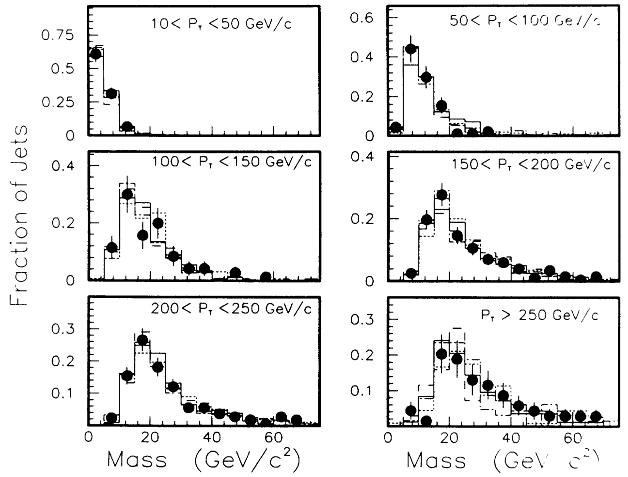

FIG. 16. Distribution of single-jet masses (as defined in the text) shown for six different regions of jet transverse momenta. The data (points) are compared with HERWIG predictions using the DO1 (solid line), DO2 (short dashed line), EHLQ1 (long dashed line), and EHLQ2 (dot-dashed line) structure functions, and the scale $Q^2=2stu/(s^2+t^2+u^2)$.

XI. MULTIJET RATES AND PROPERTIES

The observed uncorrected jet multiplicity distributions are shown in Fig. 17 as a function of the p_T threshold above which we count jets. The agreement with QCD expectations is reasonable. The initial- and final-state gluon bremsstrahlung model implemented in HERWIG appears to give a reasonable description of the rate of additional jets arising from higher-order processes. The predictions are not sensitive to choice of structure function, Q^2 scale, calorimeter response, or HERWIG version. We note that the Monte Carlo calculation does not include contributions to jet production from double-parton interactions. However, this contribution is expected to be small. A naive estimate is obtained by noting that we find on average 0.012 jets per minimum-bias event with jet-$p_T>10$ GeV/c and $|\eta|<2$, and assuming that this same fraction of high-$\sum E_T$ events contains a second parton-parton interaction which produces an observed jet ($p_T>10$ GeV/c and $|\eta|<2$). We would then expect only three jets in our event sample to arise from this source.

We next define the variables H_n which give the fraction of the total $\sum E_T$ in an event which is attributable to the sum of the n highest-p_T jets:

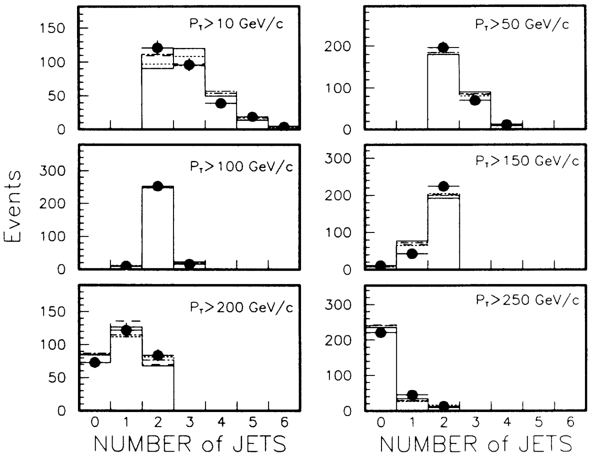

FIG. 17. Jet multiplicity distributions shown for jets with pseudorapidity $|\eta|<2.0$. The six plots correspond to the six different transverse-momentum thresholds as indicated. The data (points) are compared with HERWIG predictions normalized to the data and using the DO1 (solid line), DO2 (short dashed line), EHLQ1 (long dashed line), and EHLQ2 (dot-dashed line) structure functions, and the scale $Q^2=2stu/(s^2+t^2+u^2)$. Note that at high jet transverse-momentum threshold the jet multiplicity distributions reflect two-jet dominance together with the $\sum E_T>400$ GeV requirement.

$$H_n \equiv \frac{\sum_{j=1}^{n} E_{T_j}}{\sum E_T} .$$

No p_T or $|\eta|$ cuts were applied to the jets used in computing the H_n. Note that H_1 and H_2 were used [11,12] to demonstrate two-jet dominance in high-$\sum E_T$ events at the CERN proton-antiproton collider. H_1, H_2, H_3, and H_4 distributions are shown in Fig. 18. As expected H_1 peaks at 0.5 and H_2 at 1.0, demonstrating the expected two-jet dominance. The agreement with the QCD predictions is reasonable. The measured H_3 and H_4 distributions are less strongly peaked towards 1.0 than the predictions, which may indicate the need for a higher-order QCD calculation. However, the difference is small. Note that the level of disagreement corresponds to a discrepancy of the order of 10 GeV of unclustered E_T in events with $\sum E_T > 400$ GeV.

The two-jet, three-jet, four-jet, and five-jet mass distributions are shown in Fig. 19 for those events containing exactly two, three, four, and five jets with $p_T > 10$ GeV and $|\eta| < 2$. The agreement with the QCD expectations is good. There is no significant evidence for any unexpected structure in any of the mass plots.

XII. SUMMARY

We have selected $p\bar{p}$ interactions with observed $\sum E_T > 400$ GeV and compared the detailed properties of the high-$\sum E_T$ events with QCD expectations together with a simulation of the CDF detector. There are 279 events in the $\sum E_T > 400$ GeV sample which corresponds to an integrated luminosity of 4.0±0.3 pb^{-1}.

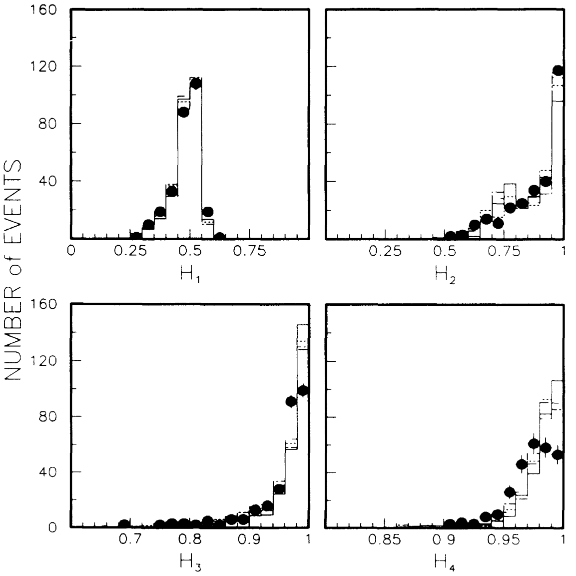

FIG. 18. Distributions of H_1, H_2, H_3, and H_4 as defined in the text. The data (points) are compared with HERWIG predictions normalized to the data and using the DO1 (solid line), DO2 (short dashed line), EHLQ1 (long dashed line), and EHLQ2 (dot-dashed line) structure functions, and the scale $Q^2 = 2stu/(s^2+t^2+u^2)$.

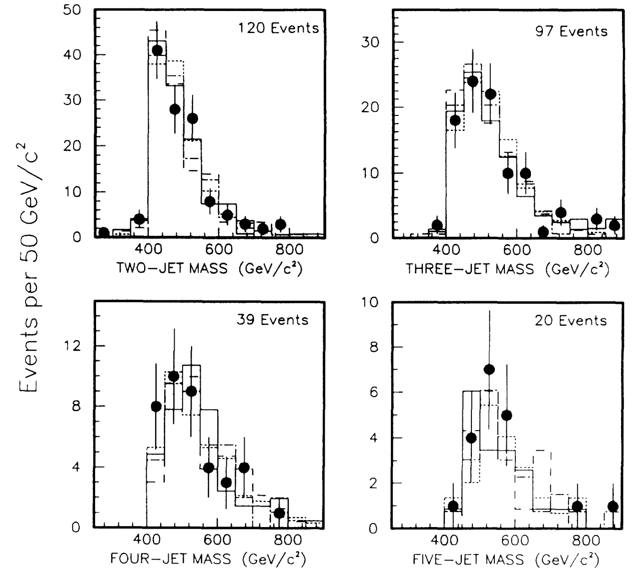

FIG. 19. Multijet mass distributions for two-jet, three-jet, four-jet, and five-jet events, where jets are counted having transverse momentum greater than 10 GeV, and pseudorapidity $|\eta| < 2.0$. The data (points) are compared with HERWIG predictions normalized to the data and using the DO1 (solid line), DO2 (short dashed line), EHLQ1 (long dashed line), and EHLQ2 (dot-dashed line) structure functions, and the scale $Q^2 = 2stu/(s^2+t^2+u^2)$.

The observed event rate is consistent with the QCD predictions. The observed distributions of jet multiplicity, jet-p_T, jet-η, the fraction of the event $\sum E_T$ associated with the one- and two-highest-p_T jets, and the two-jet, three-jet, four-jet, and five-jet mass distributions are well described by expectations based on leading-order QCD together with the gluon radiation model implemented in the HERWIG Monte Carlo program. Although we have not tuned HERWIG on CDF data, the QCD Monte Carlo calculation gives a satisfactory description of the observed jet shapes and single-jet masses. There is no evidence for a separate population of fat jets, or jets with high mass.

We see no clear evidence in the high-$\sum E_T$ event sample for any deviation from standard-model expectations. In particular there is no evidence for an excess of isolated high-p_T electrons, muons, or τ leptons. Furthermore, the agreement between the observed and predicted missing-E_T distributions show no evidence for an excess of high-p_T neutrinos. We have identified several isolated high-p_T photon candidates in the sample which are consistent with expectations from direct photon production and from jet fluctuations into one or more leading neutral pions which fake an isolated photon in the detector. There is also one spectacular diphoton even in the sample.

ACKNOWLEDGMENTS

We thank the Fermilab Accelerator Division staff and the CDF support staff for their dedicated effort that made this experiment possible. This work was supported by the Department of Energy, the National Science Foundation, Istituto Nazionale di Fisica Nucleare, the Ministry of Science, Culture and Education of Japan, and the A.P. Sloan Foundation.

[1] CDF Collaboration, F. Abe *et al.*, Nucl. Instrum. Methods **A271**, 387 (1988).

[2] CDF Collaboration, F. Abe *et al.*, Phys. Rev. D **45**, 1448 (1992).

[3] G. Marchesini and B. R. Webber, Nucl. Phys. **B310**, 461 (1988).

[4] D. W. Duke and J. F. Owens, Phys. Rev. D **30**, 49 (1984).

[5] E. Eichten, I. Hinchliffe, K. Lane, and C. Quigg, Rev. Mod. Phys. **56**, 579 (1984); **58**, 1065 (1986).

[6] CDF Collaboration, M. Franklin, in *Proceedings of the Seventh Topical Workshop on Proton-Antiproton Collider Physics,* Batavia, Illinois, 1988, edited by R. Raja and J. Yoh (Fermilab, Batavia, 1988).

[7] CDF Collaboration, F. Abe *et al.*, Phys. Rev. Lett. **62**, 1825 (1989).

[8] CDF Collaboration, F. Abe *et al.*, Phys. Rev. Lett. **67**, 2937 (1991).

[9] CDF Collaboration, F. Abe *et al.*, Phys. Rev. Lett. **64**, 157 (1990).

[10] UA1 Collaboration, G. Arnison *et al.*, CERN Report No. CERN-EP/85-116 (unpublished).

[11] UA2 Collaboration, J. A. Appel *et al.*, Phys. Lett. **165B**, 441 (1985).

[12] UA1 Collaboration, C. Albajar *et al.*, Z. Phys. C **36**, 33 (1987).

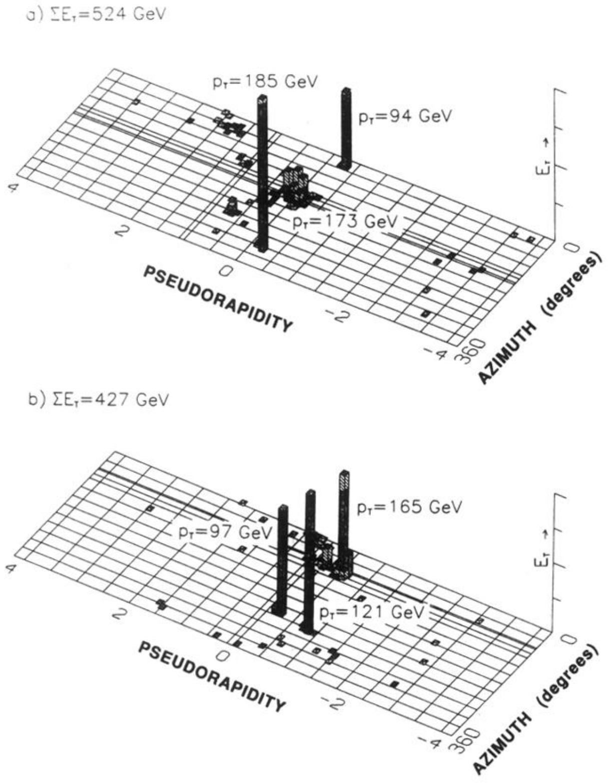

FIG. 10. Energy flow in the transverse plane for (a) the $\gamma\gamma$ +jets candidate event, and (b) the e^+e^- + jets candidate event.

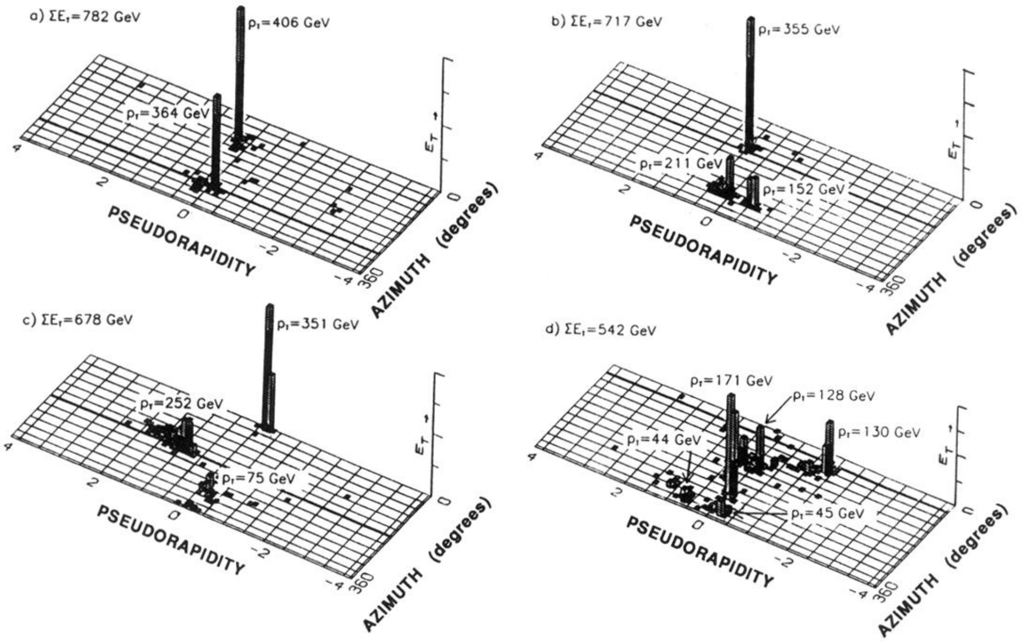

FIG. 9. Energy flow in the transverse plane for the three events containing the highest total transverse energies [(a)–(c)] observed in the CDF high-$\sum E_T$ data sample, and (d) an example of an event with a complicated jet topology.